厚生労働科学研究費補助金

長寿科学総合研究事業

血中脂質メディエータを標的とした
新規の骨粗鬆症治療薬の開発とその臨床応用

平成２１年度　総括研究報告書

研究代表者　　石井　優

平成２２（２０１０）年　４月

別添１

厚生労働科学研究費補助金

長寿科学総合研究事業

血中脂質メディエータを標的とした
新規の骨粗鬆症治療薬の開発とその臨床応用

平成２１年度　総括研究報告書

研究代表者　　石井　優

平成２２（２０１０）年　４月

別添２

目　　次

Ⅰ．総括研究報告
血中脂質メディエーターを標的とした新規の骨粗鬆症治療薬の開発と
その臨床応用 ---------- 1
石井　優
（資料）資料名

Ⅱ．研究成果の刊行に関する一覧表 ---------- 5

Ⅲ．研究成果の刊行物･別刷 ---------- 6

別添３

厚生労働科学研究費補助金（長寿総合研究事業）
（総括）研究報告書

血中脂質メディエーターを標的とした新規の骨粗鬆症治療薬の開発とその臨床応用

研究代表者　石井　優　大阪大学免疫学フロンティア研究センター准教授

研究要旨

超高齢時代を迎えた日本では、加齢による骨粗鬆症の罹患者数は 1000 万人を突破しつつある。骨組織は、古い骨を壊して吸収する「破骨細胞」と、骨を新生する「骨芽細胞」のバランスの取れた働きによって恒常性が維持されているが、炎症や加齢により破骨細胞の機能が亢進するとバランスが骨吸収側に傾き骨粗鬆症の発症へとつながる。近年、破骨細胞を標的とした骨吸収抑制剤が開発され、特に終分化した破骨細胞の機能を阻害するビスホスフォネート(BP)製剤が骨吸収抑制剤として臨床現場で汎用されている。これらの薬剤はその有効性が十分示されているものの骨粗鬆症の進行を完全に抑制するには至らず、新規の骨吸収抑制薬の開発、特に現有する BP 製剤と作用機序が大きく異なり、併用により優れた相乗効果が期待できる新規薬物の開発が切望されている。研究代表者は最近、米国国立衛生学研究所(NIH)での国際共同研究により、破骨細胞の単球系前駆細胞が骨表面へ遊走し接着する段階に注目し、血中の脂質メディエーターであるスフィンゴシン1リン酸(S1P)がこの過程を制御することを明らかにした。さらに、新規の免疫抑制剤として注目されているS1P 作動物質であるFTY720 が、強力な骨吸収抑制作用をもつことを動物実験により明らかにした(Nature, *in press*)。この薬物は既存の BP 製剤などとは作用機序が異なるので、併用により相乗的な薬効が得られることが期待される。本研究では、FTY720 やその他の臨床応用可能な S1P 作動薬（KRP-203, LX2931)に注目し、卵巣摘出などの骨粗鬆症モデルマウスを用いて、これら薬剤の骨吸収抑制効果について検討する。また、すでに免疫抑制剤として臨床治験中のこれら S1P 作用薬についての臨床データを収集・抽出し、その骨粗鬆症治療・予防効果について後ろ向き解析を行うと同時に、将来的な新規骨吸収抑制薬としての臨床応用に向けて、治療介入試験に向けた準備を積極的に行っていく。

A.研究目的

2005年に日本は総人口の約30%が65歳以上、中でも 75 歳以上の後期高齢者が全体の約10%という世界でも屈指の長寿大国となった。しかも今後高齢化は一層進行し、2050 年には 65 歳以上の人口が 40%（75 歳以上が 25%）に達すると予想されている（平成 19 年度・高齢社会白書・人口推計より)。一方で、医療技術の進歩により高齢であっても健康で生産的な生活を過ごす人の割合が増加傾向にあるが、これを阻む大きな要因として加齢による骨粗鬆症が挙げられる（長期臥床の原因として全体の約 15～20%)。実際、現在 65 歳以上では約３割以上（総計で約 1000 万人）が骨粗鬆症を罹患していると考えられており、高齢社会白書での人口推計と対照すると、2050 年には骨粗鬆症患者の総数は 5000 万人を越える可能性があり、有効な骨粗鬆症対策は２１世紀の日本の医療にとって緊要の課題である。

近年、単球・マクロファージ系血液細胞から分化・成熟する破骨細胞が、骨粗鬆症の病理形成に中心的な役割を果たしていることが

示され、これを標的とするビスホスフォネート製剤(BP)が骨吸収抑制剤として広く臨床応用されている。これまでに複数の有効なBP 製剤が開発されているが、いずれも最終分化した成熟破骨細胞の機能を抑制する点で基本的には作用機序が同一であり、複数の併用による相乗効果は期待できなかった。本研究代表者は、特殊なイメージング技術を駆使して骨組織内を生きたままの状態で観察することに世界に先駆けて成功し、これにより破骨細胞前駆細胞が血中から骨組織へ侵入したり、逆に血中へと再還流する様子を直視下に捉えることに成功した。さらにこの実験系を用いて、血中の脂質メディエーターの１種であるスフィンゴシン１リン酸（S1P）が破骨細胞前駆細胞を（成熟する前に）血中へと引き戻す役割を担っていることを明らかにしていた。今回の計画研究の目的は、この研究代表者のこれまでの研究成果を元にして、S1P を標的とした新しい骨吸収抑制剤の開発の可能性について検討することであった。

B.研究方法

破骨細胞前駆細胞の血中への再還流は、S1P に対して正の作用をもつ $S1P_1$ 受容体と、負の作用をもつ $S1P_2$ 受容体のバランスによって決定されている。本研究では ①$S1P_1$ アゴニスト と ②$S1P_2$ アンタゴニスト について、骨粗鬆症モデルマウスを用いた治療実験により骨吸収抑制効果を検討した。具体的には、卵巣摘出骨粗鬆症誘導マウスに対し、①$S1P_1$ のアゴニストとしては SEW2871（研究試薬）と FTY720（現在、免疫抑制剤として米国で臨床治験中-Phase III）を、$S1P_2$ 受容体のアンタゴニストとしては JTE013（研究試薬）を、それぞれ卵巣摘出と同時にまたは摘出後一定期間後より、1mg/kg, 3mg/kg, 10mg/kg の３つの用量で投与し、４週間後に屠殺し骨組織を解析した。骨組織および薬効の評価には、高解像度μCT による骨形態計測および末梢血 DPD 測定による骨代謝マーカーの変動評価に加え、研究代表者が独自に開発した骨組織内の生体ライブイメージングを駆使して、破骨細胞前駆細胞に対する薬剤の効果についても検討を加える。

（倫理面への配慮）

実験マウスを用いた実験を行う本研究を遂行するにあたっては、「動物の愛護および管理に関する法律」「実験動物の飼育及び保管並びに苦痛の軽減に関する基準」「厚生労働省の所管する実験施設における動物実験等の実施に関する基本指針」など、関連法規・指針に従った必要な措置を講じ、同センターでの実験動物利用指針に準拠し、動物愛護上の観点に十分配慮した環境で行う。また、本申請研究は、患者臨床検体や人体生体材料などは用いない形で施行予定であり、臨床治験の公開データよりデータマイニングによる検討を行う場合には、研究対象者に不利益・危険性を及ぶ可能性は低い。ただ、臨床経過についてより詳細な結果を、製薬企業に提供を求めて行う場合には、当センターの COI 委員会（外部専門委員を含む）の指示の下、十分な配慮を行う。

C.D.研究結果と考察

まず、卵巣摘出骨粗鬆症モデルマウスにおいて、卵巣摘出と同時に SEW2871 または FTY720 を投与し、４週間後に骨組織を解析したものでは、SEW2871 に関しては 1mg/kg, 3mg/kg, 10mg/kg 投与群のいずれにおいても、骨密度に有意な変化は見られなかったが、FTY720 投与群では 1mg/kg では効果はないものの、3mg/kg, 10mg/kg 投与群では有意な骨吸収抑制効果が認められた。一方 3mg/kg と 10mg/kg 投与群では効果に有意な差は認めなかった。次に、卵巣摘出の１週間後より FTY720 3mg/kg を投与した場合、その３週間後の解析では、vehicle 投与群に比べて骨密度が有意に回復しており、FTY720 などの $S1P_1$ を標的とした治療は、骨粗鬆症の予防のみな

らず治療薬としても有望であることが示された。

さらに既述の通り、本研究代表者は、破骨細胞前駆細胞には S1P に対して遊走を起こす $S1P_1$ 受容体に加えて、これを抑制する $S1P_2$ 受容体が同時に発現していることを発見している。本研究ではこの負の受容体である $S1P_2$ を抑制して、結果として $S1P_1$ 作用を強化することにより、骨吸収が抑制できないかについても解析した。現在、$S1P_2$ 受容体のアンタゴニストとして JTE013 が存在するが、本研究ではこれを卵巣摘出モデルマウスに投与する実験を行った。卵巣摘出骨粗鬆症モデルマウスにおいて、卵巣摘出と同時に JTE013 を投与し、4 週間後に骨組織を解析した。この結果、JTE013 投与群では 1mg/kg, 3mg/kg で極めて強力な骨吸収抑制効果が認められた。これらの結果から、S1P 作用を標的とする破骨細胞前駆細胞の遊走制御は、新しい骨粗鬆症治療薬として極めて有望であることが示された。

E.結論

超高齢社会を迎えた本邦では、より安全性・有効性の高い骨粗鬆症治療法の開発は喫緊の課題である。本研究では、S1P による破骨前駆細胞の遊走・位置決めを標的とした、これまでとは全く異なるコンセプトによる新規の骨粗鬆症治療薬の開発へ道を拓くものであり、その社会的意義は大きい。これらの薬剤は破骨細胞前駆細胞の骨組織への流入出バランスという、内因性の調節機転を利用するため、ビスフォスホネート(BP)製剤のように、古い骨の吸収を強力に抑制しすぎるために起きうる顎骨壊死などの重篤な副作用が少ないことが期待される。また BP 製剤と全く異なる薬効作用点を持っているため、併用による相乗効果も期待されるので、重症の骨粗鬆症に対しては併用による強力な治療が可能となる他、これまで BP 製剤を使用していた症例に対しても、本研究で開発する新治療薬との併用により内服する BP 製剤の容量を抑えることにより顎骨壊死などの副作用のリスクを下げることが可能となる。

本研究では骨粗鬆症モデル動物を用いた実験により、$S1P_1$ 受容体アゴニストおよび $S1P_2$ 受容体アンタゴニストが骨吸収抑制に極めて有用であることが示された。特に、$S1P_2$ は、$S1P_1$ とは異なり発現が単球系細胞(破骨細胞)に比較的特異的であるため、副作用が少ない優れた薬剤として開発できる可能性がある。本研究代表者はすでに国内の製薬メーカーと本研究成果について打ち合わせをしており、今後 $S1P_2$ アンタゴニストを主たる薬効とする新規骨粗鬆症治療薬の開発を行っていく計画としている。

破骨細胞前駆細胞が血中から遊走し骨へと位置決めをするシステムが、血中 S1P によって動的に調節されていることを示した研究代表者の研究は独創性・新規性が極めて高く、骨代謝におけるパラダイムシフトを引き起こしており、この新概念に基づいた、新規の骨粗鬆症治療薬開発を目指す本研究は、世界的にも類を見ないオリジナルな課題である。社会の高齢化および骨吸収性疾患の増加は、日本に限ったものではなく先進諸国に共通した問題である。現在、骨粗鬆症の罹患者数は日米欧の先進諸国において約 7500 万人と推定されており、BP 製剤を初めとする骨吸収抑制剤の世界市場は総額 8000 億円に及ぶ巨大なマーケットである。しかも、世界規模の少子高齢化時代に向け、この市場は今後確実に増加することが予想される。このため、本研究の保健医療における意義は日本国内に留まらず、世界での新たな疾患治療モデルを提唱すると同時に、日本発で世界を牽引する創薬ビジネスのチャンスとも考えられる。

G.研究発表

1．論文発表

1) **Ishii M**, Egen JG, Klauschen F, Meier-Schellersheim M, Saeki Y, Vacher J, Proia RL, Germain RN. (2009)

Sphingosine-1-phosphate mobilizes osteoclast precursors and regulates bone homeostasis. ***Nature***, 458 (7237): 524-528.

2) Klauschen F, **Ishii M**, Qi H, Bajénoff M, Egen JG, Germain RN, Meier-Schellersheim M. (2009) Quantifying cellular interaction dynamics in 3-D fluorescence microscopy data. ***Nature Protoc.,*** 4(9): 1305-1311.

3) Mazzucchelli R, Warming S, Lawrence SM, **Ishii M**, Abshari M, Feigenbaum L, Washington AV, Warner AC, Sims DJ, Li WQ, Hixon JA, Gray DHD, Rich BE, Morrow M, Anver MR, Cherry J, Naf D, Sternberg LR, McVicar DW, Farr AG, Germain RN, Rogers K, Copeland N, Durum SK. (2009) Visualization and identification of IL-7 producing cells in reporter mice. ***PLoS One***, 4(11): e7637.

4) 石井　優,「破骨細胞前駆細胞の遊走・局在制御～ニ光子励起顕微鏡を用いた骨免疫イメージングより～,「The Bone」23 巻 4 号, 427-432（2009）

5) 石井　優,「脂質メディエーターによる破骨細胞前駆細胞の遊走・位置決めの制御～生体ニ光子励起顕微鏡を用いた骨組織の in vivo イメージングより～」「感染・炎症・免疫」39 巻 3 号, 210-217（2009）

6) 石井　優,「骨組織のライブイメージングにより明らかとなった破骨細胞の遊走と位置決めの制御」,「最新医学」64 巻 12 号, 2621-2626（2009）

7) 石井　優,「骨組織・骨髄内の２光子励起ライブイメージング」, 医学のあゆみ　232 巻 13 号, 1247-1252（2010）

２．学会発表

1) The 14th International Conferences on Endocrinology 2010 (ICE2010)・サテライトシンポジウム・招待講演（2010 年 3 月 31 日・大阪）

2) The 14th International Conferences on Endocrinology 2010 (ICE2010)シンポジウム講演（2010 年 3 月 26 日・京都）

3) 第 83 日本薬理学会年会・シンポジウム講演（2010 年 3 月 16 日・大阪）

4) International Bone and Mineral Society (IBMS), Davos Workshops, 招待講演 (2010 年 3 月 14 日・ダヴォス（スイス））

5) 第 31 日本分子生物学会大会・ワークショップ講演（2009 年 12 月 12 日・横浜）

6) 第 39 日本免疫学会大会・シンポジウム講演（2009 年 12 月 3 日・大阪）

7) 第 82 回・日本生化学会大会・シンポジウム講演（2009 年 10 月 23 日・神戸）

8) 6th Bone Biology Forum・招待講演（2008 年 8 月 21 日・静岡県裾野市）

9) 第 27 回・日本骨代謝学会・シンポジウムおよび Meet-the-Expert 講演（2009 年 7 月 24 日）

10) 免疫サマースクール 2009・招待講演（2009 年 7 月 16 日・淡路）

11) 第 3 回・GCOE 国際シンポジウム・招待講演（2009 年 6 月 11 日・東京医科歯科大学）

12) PLM2009（国際学会）・シンポジウム講演（2009 年 5 月 27 日・東京）

H.知的財産権の出願・登録状況
（予定を含む。）

１．特許取得

＜出願中（1 件）＞

名称：新規骨吸収抑制剤のスクリーニング方法
発明者：石井　優
権利者：国立大学法人大阪大学
種類：特許権
番号：特願 2009-260655
出願年月日：2009 年 11 月 16 日

２．実用新案登録

該当なし

３．その他

該当なし

別添４

研究成果の刊行に関する一覧表

雑誌

発表者氏名	論文タイトル名	発表誌名	巻号	ページ	出版年
石井　優　他	Sphingosine-1-phosphate mobilizes osteoclast-precursors and regulates bone homeostasis.	Nature	458・7237	524-528	2009
石井　優、他	Quantifying cellular interaction dynamics in 3-D fluorescence microscopy data.	Nature Protoc.,	4・9	1305-1311	2009
石井　優、他	Visualization and identification of IL-7 producing cells in reporter mice.	PLoS One	4・11	e7637	2009
石井　優	破骨細胞前駆細胞の遊走・局在制御～ニ光子励起顕微鏡を用いた骨免疫イメージングより～	The Bone	23・4	427-432	2009
石井　優	脂質メディエーターによる破骨細胞前駆細胞の遊走・位置決めの制御～生体ニ光子励起顕微鏡を用いた骨組織のin vivoイメージングより～	感染・炎症・免疫	39・3	210-217	2009
石井　優	骨組織のライブイメージングにより明らかとなった破骨細胞の遊走と位置決めの制御	最新医学	64・12	2621-2626	2009
石井　優	骨組織・骨髄内の２光子励起ライブイメージング	医学のあゆみ	232・13	1247-1252	2010

nature

Vol 458|26 March 2009|doi:10.1038/nature07713

LETTERS

Sphingosine-1-phosphate mobilizes osteoclast precursors and regulates bone homeostasis

Masaru Ishii[1,4,5], Jackson G. Egen[1], Frederick Klauschen[2], Martin Meier-Schellersheim[2], Yukihiko Saeki[5], Jean Vacher[6], Richard L. Proia[3] & Ronald N. Germain[1,2]

Osteoclasts are the only somatic cells with bone-resorbing capacity and, as such, they have a critical role not only in normal bone homeostasis (called 'bone remodelling') but also in the pathogenesis of bone destructive disorders such as rheumatoid arthritis and osteoporosis[1]. A major focus of research in the field has been on gene regulation by osteoclastogenic cytokines such as receptor activator of NF-κB-ligand (RANKL, also known as TNFSF11) and TNF-α, both of which have been well documented to contribute to osteoclast terminal differentiation[2,3]. A crucial process that has been less well studied is the trafficking of osteoclast precursors to and from the bone surface, where they undergo cell fusion to form the fully differentiated multinucleated cells that mediate bone resorption. Here we report that sphingosine-1-phosphate (S1P), a lipid mediator enriched in blood[4,5], induces chemotaxis and regulates the migration of osteoclast precursors not only in culture but also *in vivo*, contributing to the dynamic control of bone mineral homeostasis. Cells with the properties of osteoclast precursors express functional $S1P_1$ receptors and exhibit positive chemotaxis along an S1P gradient *in vitro*. Intravital two-photon imaging of bone tissues showed that a potent $S1P_1$ agonist, SEW2871, stimulated motility of osteoclast precursor-containing monocytoid populations *in vivo*. Osteoclast/monocyte (CD11b, also known as ITGAM) lineage-specific conditional $S1P_1$ knockout mice showed osteoporotic changes due to increased osteoclast attachment to the bone surface. Furthermore, treatment with the $S1P_1$ agonist FTY720 relieved ovariectomy-induced osteoporosis in mice by reducing the number of mature osteoclasts attached to the bone surface. Together, these data provide evidence that S1P controls the migratory behaviour of osteoclast precursors, dynamically regulating bone mineral homeostasis, and identifies a critical control point in osteoclastogenesis that may have potential as a therapeutic target.

Because of its role in controlling cell migration in other tissues, we initially focused on S1P and the S1P family of receptors (previously known as EDG receptors) responsive to this lipid mediator. The murine monocyte cell line RAW264.7, and mouse bone-marrow-derived M-CSF (colony stimulating factor-1, also known as CSF1)-dependent monocytes (termed BM-MDM), which can both differentiate into osteoclast-like cells on exposure to RANKL and represent widely used *in vitro* models of osteoclast precursors, each express messenger RNAs encoding two receptors for S1P ($S1P_1$ and $S1P_2$, encoded by *S1PR1* and *S1PR2*, respectively.). The expression of *S1PR1* mRNA decreased after RANKL stimulation (Fig. 1a, b), and this transcriptional repression was dependent on NF-κB (blocked by BAY11-7085) but not on NF-AT (also known as NFATC1; blocked by cyclosporin A) (Fig. 1b), both of which have been recognized as crucial transcriptional factors for osteoclastogenesis[1–3]. $S1P_1$ protein expression, as detected by immunocytochemistry, was also reduced by RANKL stimulation (Fig. 1c). In accord with these *in vitro* findings, strong immunoreactivity for $S1P_1$ could be detected in mononuclear cells in native bone tissues (Fig. 1d, arrowheads), whereas weaker staining was seen in large cells lining bone trabeculae (Fig. 1d, asterisks) that are probably mature osteoclasts (mean fluorescence intensities: 49.1 ± 5.8 and 19.4 ± 2.0 in mononuclear cells and attached cells, respectively; $P = 0.0003$). Both RAW264.7 (Fig. 1f) and BM-MDM (data not shown) cells showed positive chemotactic responses to an S1P gradient *in vitro*, and these responses were greatly attenuated by pretreatment with RANKL (Fig. 1f). This latter finding is concordant with the RANKL-dependent reduction in *S1PR1* gene expression (Fig. 1a). S1P-directed chemotaxis was blocked by pertussis toxin (PTX)[6] and NSC23766 (ref. 7) (Fig. 1f), and S1P induced an increase in the GTP-bound, active form of Rac (GTP-Rac) (Fig. 1e), suggesting that Rac and the adenylyl-cyclase-inhibiting G protein $G\alpha_i$ are involved in the $S1P_1$ chemotactic signalling pathway in these cells, consistent with previous reports[8,9]. *In vitro* chemotaxis of RAW264.7 was also examined using a dynamic imaging approach, in which cells could be observed vigorously migrating towards S1P-containing medium (Fig. 1g and Supplementary Videos 1 and 2). We also detected S1P-induced upregulation of integrins expressed in monocytoid cells, suggesting that S1P-mediated alterations in cell adhesion could contribute to chemotaxis *in vivo* (Supplementary Fig. 1).

To investigate whether osteoclast precursor migration is affected by S1P gradients *in vivo*, we performed intravital two-photon imaging of calvaria bone tissues[10,11] and examined the migratory behaviour of monocytoid cells containing osteoclast precursors resident in the marrow spaces. We used two strains of mice expressing enhanced green fluorescent protein (EGFP) in subsets of myeloid cells: CX_3CR1–EGFP knock-in (heterozygous) mice[12,13] and CSF1R–EGFP transgenic mice[14]. In both strains, haematopoietic monocyte-lineage cell types predominantly expressed EGFP[12,13] and we confirmed that tartrate-resistant acid phosphatase (TRAP)-positive mature osteoclasts expressed EGFP in these animals (Supplementary Fig. 2), suggesting that $EGFP^+$ cells contain osteoclast precursor monocytes. Nearly two-thirds of CX_3CR1–EGFP cells and half of CSF1R–EGFP cells express RANK (also known as TNFRSF11A), a receptor for RANKL (Supplementary Table 1), suggesting that there is a capacity for many of the fluorescent cells to differentiate into mature osteoclasts.

CX_3CR1–EGFP-positive cells present in bone marrow stromal locations or at the bone surface and not in the blood sinusoidal spaces were generally stationary under control conditions (Fig. 2a, upper panels

[1]Lymphocyte Biology Section, Laboratory of Immunology, [2]Program in Systems Immunology and Infectious Disease Modeling, National Institute of Allergy and Infectious Diseases, and [3]Genetics of Development and Disease Branch, National Institute of Diabetes and Digestive and Kidney Diseases, National Institutes of Health, Bethesda, Maryland 20892-1892, USA. [4]Laboratory of Biological Imaging, WPI-Immunology Frontier Research Center, Osaka University, Osaka 565-0871, Japan. [5]Department of Clinical Research, National Osaka Minami Medical Center, Osaka 586-8521, Japan. [6]Institut de Recherches Cliniques de Montréal, Quebec H2W 1R7, Canada.

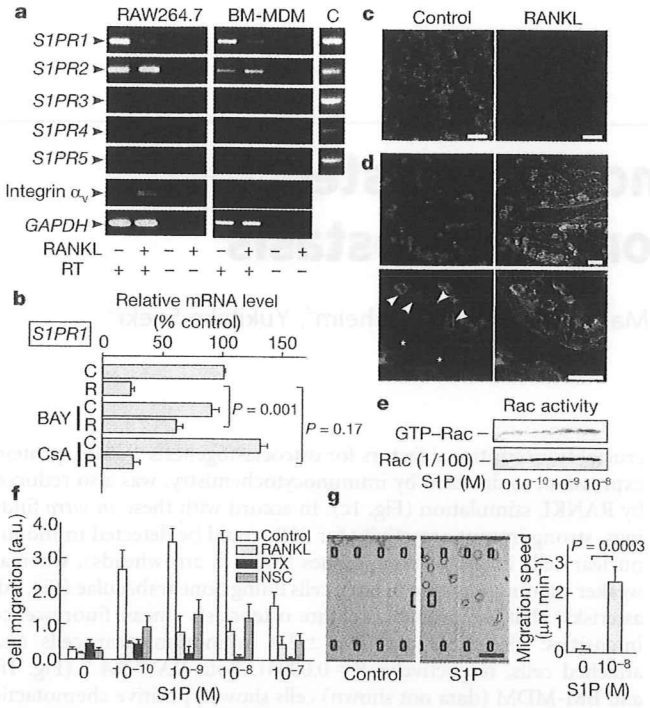

Figure 1 | Expression and function of S1P receptors in osteoclast precursor monocytes. **a**, Expression of mRNAs encoding 5 mammalian S1P receptors ($S1P_1$ to $S1P_5$, encoded by *S1PR1* to *S1PR5*) in RAW264.7 monocytes (left panels) and in mouse BM-MDM (middle panels), detected by RT–PCR. mRNAs for integrin α_v and *GAPDH* were also analysed as controls. Total complementary DNA isolated from mouse thymus was used for positive controls (C, right panels). RT, reverse transcription. **b**, qRT–PCR analysis of *S1PR1* mRNA expressed in RAW264.7 cells cultured in the absence (C) or presence (R) of RANKL. Cells were treated with BAY11-7085 (BAY; 10 μM) or cyclosporine A (CsA; 1 μM). Error bars represent s.e.m. **c**, Immunofluorescent detection of $S1P_1$ protein (green) in RAW264.7 cells cultured in the absence (left panel) or presence (right panel) of 50 ng ml^{-1} RANKL. Nuclei were visualized with propidium iodide (red). **d**, Immunohistochemical analysis of $S1P_1$ in mouse femoral bone tissues at low (top) and high (bottom) magnification. Staining for $S1P_1$ (green; left two panels) and a merged image with staining for CD9 (red) and transmission (Nomarski image) (right two panels) are shown. Arrowheads represent $S1P_1^{high}$ mononuclear cells adjacent to bone trabeculae (asterisk). Scale bars in **c** and **d**, 20 μm. **e**, S1P-induced Rac stimulation. RAW264.7 cells were treated with various concentrations of S1P for 15 min and then analysed for GTP-Rac. **f**, *In vitro* chemotactic response of RAW264.7 to S1P gradient. Error bars represent s.e.m. ($n = 6$). **g**, *In vitro* S1P-directed chemotaxis of RAW264.7 dynamically visualized using EZ-Taxiscan. Cells were loaded onto the upper chamber and the lower chamber was filled either with normal medium (right panel; Supplementary Video 1) or with medium containing 10^{-8} M S1P (middle panel; Supplementary Video 2). Mean migration speed is shown in right panel. Error bars represent s.e.m. ($n = 8$). Scale bar represents 100 μm.

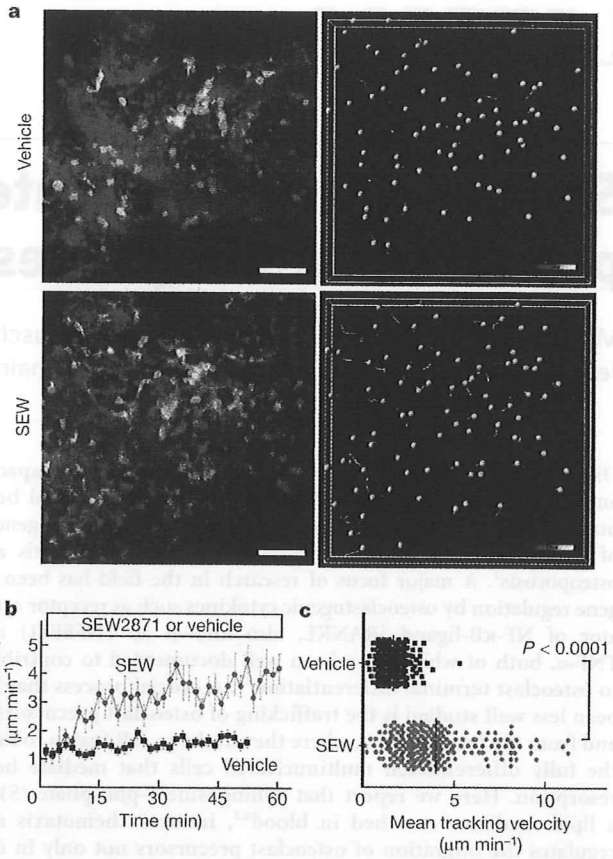

Figure 2 | *In vivo* S1P-mediated increase in motility of osteoclast precursor monocytes visualized using intravital two-photon imaging. **a**, Intravital two-photon imaging of mouse skull bone tissues of heterozygous CX_3CR1–EGFP knock-in mice, in the absence (top panels; Supplementary Video 3) or presence (bottom panels; Supplementary Video 4) of the $S1P_1$ agonist SEW2871 (SEW; 5 mg kg^{-1}). CX_3CR1–EGFP-positive cells appear green. The microvasculature was visualized by intravenous injection of 70 kDa dextran-conjugated Texas Red (red; left panels). The movements of CX_3CR1–EGFP positive cells were tracked for 10 min (right panels). Grey spheres represent cells and coloured lines show the associated trajectories. Scale bars represent 50 μm. **b**, Quantification of CX_3CR1–EGFP-positive cell velocity. Tracking velocity over time after application of SEW2871 (red circle) or vehicle only (black square) are shown. Data points represent mean values ± s.e.m. of cell velocities in the field at certain time points ($n = 15$ for vehicle and $n = 14$ for SEW2871). **c**, Summary of mean velocity of CX_3CR1–EGFP positive cells treated with SEW2871 (red circle) or vehicle (black circle). Data points ($n = 231$ for vehicle and $n = 210$ for SEW2871) represent individual cells compiled from five independent experiments.

and Supplementary Video 3). A subset of the labelled cells became motile shortly after the intravenous application of SEW2871 (refs 15 and 16; 5 mg kg^{-1}), a selective agonist for the $S1P_1$ receptor (Fig. 2a, lower panels, and Supplementary Video 4), with some of the mobilized cells entering the blood circulation (data not shown). A similar but less pronounced effect of SEW2871 on myeloid cell motility was observed in the bone marrow of CSF1R–EGFP transgenic mice (Supplementary Fig. 3 and Supplementary Videos 5 and 6). The difference in the fraction of cells mobilized by SEW2871 treatment in the two mouse strains is probably due to the fact that the EGFP-expressing subsets in these animals are not completely overlapping (Supplementary Table 1). Consistent with these findings, we also observed an increase in the percentage and absolute number of monocytoid cells in peripheral blood, and their reciprocal decrease in bone marrow but not spleen or liver, after SEW2871 treatment as compared to vehicle controls (Supplementary Fig. 4 and Supplementary Table 2). These results suggest that bone-marrow-resident monocytes, including many osteoclast precursors, become motile and exit marrow spaces in response to S1P stimulation.

To evaluate the *in vivo* effect of S1P-directed chemotaxis of osteoclast precursors on bone homeostasis, we examined mice deficient in $S1P_1$. Because $S1P_1$ deficiency causes embryonic lethality[17], we generated osteoclast/monocyte-specific $S1P_1$-deficient ($S1PR1^{-/-}$) mice by crossing animals bearing conditional $S1P_1$ knockout alleles ($S1PR1^{loxP}$)[18] to transgenic mice expressing Cre under the *CD11b* promoter[19], which facilitates deletion of *loxP*-flanked sequences in monocyte-lineage myeloid cells including osteoclasts. *S1PR1* mRNA was essentially undetectable by conventional and real-time quantitative PCR with reverse transcription (qRT–PCR) analyses in $CD11b^+$ myeloid cells purified from the $S1PR1^{-/-}$ mice

(Supplementary Fig. 5a, b) and immunoreactivity for $S1P_1$ was greatly diminished in *S1PR1*$^{-/-}$ bone tissues (Supplementary Fig. 5c), indicating that there was almost complete ablation of $S1P_1$ expression in this lineage.

Morphohistometric analyses using micro-CT (μCT) showed that femora of mice genotyped as *S1PR1*$^{loxP/loxP}$ *CD11b-Cre* (*S1PR1*$^{-/-}$) were osteoporotic, compared with those of control (*S1PR1*$^{+/+}$ *CD11b-Cre*) littermates (Fig. 3a, upper panels). Bone tissue density (bone volume/total volume) of *S1PR1*$^{-/-}$ mice was significantly lower than that of controls (Fig. 3b), and both trabecular thickness and trabecular density were decreased in *S1PR1*$^{-/-}$ bones (Fig. 3c). Mice genotyped as *S1PR1*$^{loxP/+}$ *CD11b-Cre* (heterozygous) were indistinguishable from controls, indicating that a single *S1PR1* allele is sufficient to sustain normal $S1P_1$-mediated functions.

Bone surface attachment of mature osteoclasts was evaluated by immunohistological examination. Both osteoclasts and bone matrices were visualized simultaneously by fluorescence-based staining for TRAP[20] and by collagen-derived second harmonic signals elicited by two-photon excitation[21], respectively (Supplementary Fig. 6). Images were automatically segmented off-line using a custom software package (F.K., submitted manuscript). An 'osteoclast attachment ratio' (bone surface occupied by osteoclasts/total bone surface) was calculated automatically without manual intervention (Fig. 3a, lower panels and Supplementary Fig. 6). The computational analyses showed that osteoclast attachment to the bone surface was significantly enhanced in *S1PR1*$^{-/-}$ animals, as compared to controls (Fig. 3d), consistent with the decrease in bone density in *S1PR1*$^{-/-}$ mice (Fig. 3b, c). Because S1P has no measurable effect on *in vitro* osteoclast differentiation stimulated by RANKL (Supplementary Fig. 7), a reasonable interpretation of these data are that the loss of $S1P_1$ function alters the chemotactic behaviour of osteoclast precursors rather than their terminal maturation to osteoclasts or the bone-resorbing action of osteoclasts.

Because the concentration of S1P in blood is higher than in tissues, S1P-mediated chemotaxis of osteoclast precursors would thus be expected to contribute to their recirculation from bone tissues to systemic blood flow, limiting formation of mature osteoclasts and reducing bone destruction. The present result showing the increased deposition of *S1PR1*$^{-/-}$ osteoclasts on the bone surface strongly supports the concept of S1P-driven precursor recirculation. It has already been reported that osteoclast precursor monocytes (RAW264.7) show positive chemotaxis *in vitro* towards CXCL12 (also known as SDF-1), a chemokine secreted from bone marrow stromal cells[22], leading to a straightforward competitive model for the migration and positioning of osteoclasts (Supplementary Fig. 8). Monocyte-lineage osteoclast precursors come close to the bone surface attracted by CXCL12, however not all of the recruited cells undergo differentiation, and some of the precursors recirculate into the blood flow owing to attraction by S1P. Some osteoclast precursors may be directly derived within bone marrow spaces (Supplementary Fig. 8, dashed arrow), and they are also susceptible to S1P-driven 'circulation' into the systemic flow. During osteoclast differentiation induced by RANKL, the expression of $S1P_1$ is repressed (Fig. 1a) which ensures stable localization of the maturing cells on the bone surface. Regulation of osteoclast generation by competing chemokine pathways that attract precursors to and from the bone surface allows finely-tuned dynamic control of osteoclastogenesis during health and in various conditions such as inflammation and metabolic disorders. Bone surface CXCL12 expression has recently been shown to be regulated by sympathetic neuron stimulation[23], suggesting that there is an interesting interaction between circulating S1P and the autonomic nervous system for the regulation of osteoclast precursor mobilization.

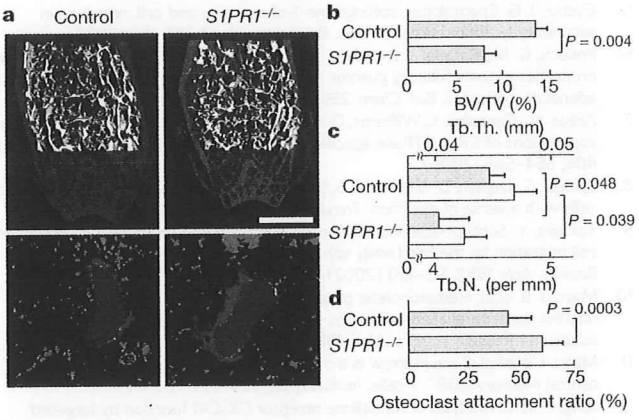

Figure 3 | *In vivo* affect of $S1P_1$ on bone mineral metabolism. **a**, Morphohistometric analyses of control and *S1PR1*$^{-/-}$ (*S1PR1*$^{loxP/loxP}$ *CD11b-Cre*) littermates. Femoral bone samples were analysed by cone-beam μCT (top panels) and by histological examination combined with computational quantification for measuring the osteoclast attachment ratio to the bone surface (bottom panels; see also Supplementary Fig. 6 and Supplementary Information). Blue areas represent bone trabeculae (second harmonic fluorescence signal), red and green areas show TRAP-positive osteoclasts that are attached to or detached from bone trabeculae, respectively, and white areas show the area of osteoclast/bone attachment. Scale bar represents 1 mm. **b–d**, Summary of the data of (**b**) bone matrix density (bone volume/total volume, BV/TV), (**c**) trabecular thickness (Tb.Th.; filled bars) and trabecular density (Tb.N.; open bars) calculated from μCT images, and (**d**) osteoclast attachment ratio calculated by computational segmentation analyses. Error bars represent s.e.m., $n = 3$ (**b**, **c**) and $n = 40$ (from 3 mice) (**d**) for each.

This newly revealed role of S1P-directed recirculation of osteoclast precursor in bone homeostasis prompted us to examine possible therapeutic implications of this regulatory pathway. FTY720 (Fingolimod) is metabolized after administration to an agonist for four of the five S1P receptors, including $S1P_1$ (but not $S1P_2$), and has emerged as a clinically promising immunosuppressive drug[24,25] that presumably acts by limiting effector lymphocyte egress from lymph nodes. FTY720 is at present being tested clinically in multiple sclerosis and allogeneic transplantation[26,27], but has not been examined for its effect on bone homeostasis. Here we show that FTY720 has a capacity to ameliorate bone loss in a model of postmenopausal osteoporosis.

Either ovariectomized or sham-operated mice were administered FTY720 (3 mg kg^{-1} day^{-1}) for 4 weeks after which excised femora were analysed by μCT (Fig. 4a, b). FTY720 treatment significantly prevented bone density loss after ovariectomy, but had no effects under control (sham-operated) conditions. Computational morphometrical analyses showed that osteoclast attachment was increased after ovariectomy and partially restored to normal levels by FTY720 administration. We confirmed that FTY720 had no effect on oestrogen levels after ovariectomy (Supplementary Table 3). These results indicate that FTY720 relieves ovariectomy-induced bone loss by reducing osteoclast deposition onto bone surfaces. This effect correlated with an increase in circulating CX_3CR1–$EGFP^+$ $F4/80^+$ (Fig. 4c) and $CD11b^+$ monocytes (Supplementary Fig. 9), both of which populations include osteoclast precursors, and a concomitant decrease in monocytoid cells including osteoclast precursors in the bone marrow (Supplementary Fig. 9 and Supplementary Table 2). In addition, intravital two-photon imaging showed that FTY720 significantly stimulated motility of CX_3CR1–$EGFP^+$ monocyte-lineage cells (Fig. 4d and Supplementary Video 7). The short-term mobility change seen using FTY720 (as observed by intravital microscopy) was less prominent than that obtained with SEW2871 (Fig. 2). This difference may arise because SEW2871 is active after intravenous injection, whereas FTY720 needs to be metabolized (phosphorylated) before becoming functional (Supplementary Fig. 10). We cannot rule out, however, the possibility that phospho-FTY720 can activate S1P receptors other than $S1P_1$ that are expressed on other cell types, such as endothelial cells. FTY720 was shown to have no effects on the expression of RANKL or osteoprotegerin (data not shown). Taken together, these results

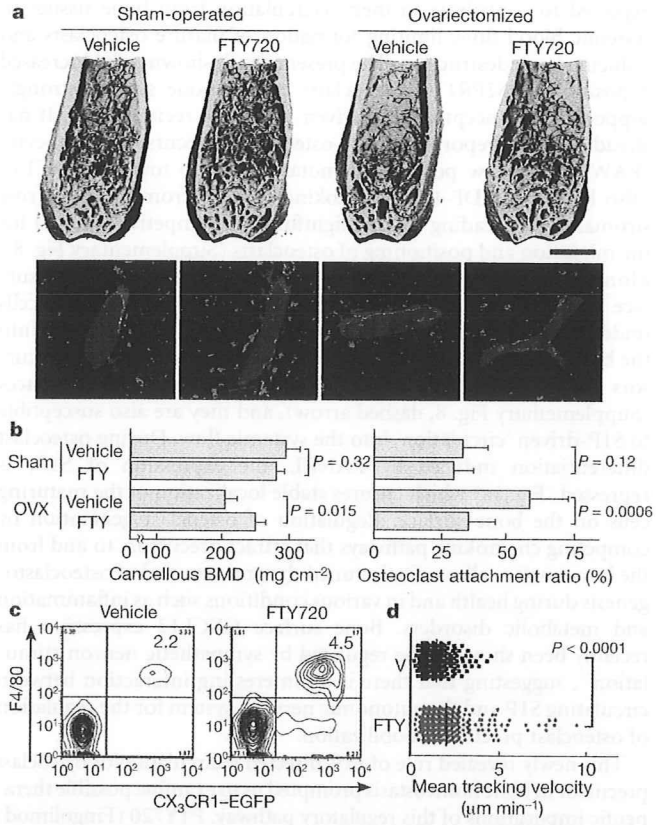

Figure 4 | Preventive effect of FTY720 on ovariectomy-induced osteoporosis. a, Effect of FTY720 on bone mineral metabolism. Femurs were collected from mice after four different treatments: sham-operated and vehicle treated, sham-operated and FTY720 treated, ovariectomized and vehicle treated, and ovariectomized and FTY720 treated. Bone samples were analysed by cone-beam μCT (top panels) and by histological examination combined with computational quantification for measuring the osteoclast attachment ratio to the bone surface (bottom panels; see Supplementary Fig. 5). Scale bar represents 1 mm. **b**, Summary of the data of cancellous bone mineral density calculated from μCT images (left panel) and of osteoclast attachment ratio (right panel). Error bars represent s.e.m., $n = 3$ (left panel) and $n = 20$ (from 3 mice; right panel) for each. **c**, Effect of FTY720 on the composition of PMCs. PMCs collected from CX_3CR1–EGFP knock-in mice administered vehicle or FTY720 were stained with anti-F4/80 (Alexa647). Absolute numbers of CX_3CR1–$EGFP^+$ $F4/80^+$ cells (per 10^5 ml of peripheral blood) are described in the panels. **d**, Effect of FTY720 on the mobility of CX_3CR1–EGFP marked cells. Summary of mean tracking velocity of CX_3CR1–EGFP-positive cells treated with FTY720 (FTY, red circles) or vehicle (V, black circles). Data points ($n = 246$ for vehicle and $n = 339$ for FTY720) represent individual cells compiled from four independent experiments. Intravital two-photon images of mouse skull bone tissues of heterozygous CX_3CR1–EGFP knock-in mice treated with FTY720 are shown in Supplementary Video 7.

indicate that FTY720, a potent $S1P_1$ agonist, promotes the recirculation of osteoclast precursor monocytes from bone surface, an effect that counteracts ovariectomy-induced augmentation of osteoclastogenesis. This agonist effect of FTY720 on myeloid cells directly accessible to the blood circulation differs from the consequence of lymphocyte $S1P_1$ engagement by phosphorylated FTY720 within secondary lymphoid tissues, in which case downmodulation of the receptor results in functional antagonism of this pathway.

The present study provides evidence that S1P, as a circulation-attraction molecule, controls the migratory behaviour of osteoclast precursors, dynamically regulating bone mineral homeostasis in collaboration with bone-attraction molecules, such as CXCL12, and identifies a critical control point in osteoclastogenesis that has potential as a therapeutic target.

METHODS SUMMARY

The RAW264.7 cell line and mouse BM-MDM cells, which contains osteoclast precursor cells, were cultured and stimulated to differentiate using RANKL as previously described[28,29]. *In vitro* chemotactic activity was evaluated using a modified Boyden's chamber[30] or with a visually-accessible chemotactic chamber, EZ-Taxiscan. *In vivo* S1P-directed chemotaxis of osteoclast precursor monocytes was visualized by intravital two-photon microscopy of mouse calvaria bone tissues of heterozygous CX_3CR1–EGFP knock-in mice[12] and of CSF1R–EGFP transgenic[14] mice, according to a protocol modified from a previous report[10,11]. The generation of the loxP-flanked *S1PR1* allele (*S1PR1*^{loxP})[18] and osteoclast/monocyte lineage-specific *CD11b-Cre* transgenic mice[19] have been described previously. Histomorphometry of femurs from osteoclast/monocyte-lineage specific $S1P_1$ conditional knockout (*S1PR1*$^{-/-}$) mice, as well as mice ovariectomized/sham-operated and treated with FTY720 or vehicle, were performed using μCT. Assessment of osteoclast attachment to the bone surface was performed using a newly developed fully automated segmentation approach to analyse two-photon images of bone tissue sections in which osteoclasts and bone trabeculae were visualized with fluorescent TRAP staining[20] and second harmonic generation from collagen fibres[21], respectively. To examine the composition of peripheral blood mononuclear cells (PMCs), the cells were stained with fluorophore-conjugated anti-F4/80, anti-CD11b and anti-CD3 using conventional methods. Flow cytometric data were collected on a FACSCalibur and analysed with FlowJo software. All mice were bred and maintained under specific pathogen-free conditions at the animal facility of the National Institutes of Health (NIH), according to NIH institutional guidelines under an approved protocol. For statistical analyses, the Mann–Whitney rank sum test was used to calculate *P* values for highly skewed distributions. For Gaussian-like distributions, two-tailed *t*-tests were used.

Full Methods and any associated references are available in the online version of the paper at www.nature.com/nature.

Received 3 September; accepted 9 December 2008.
Published online 8 February 2009.

1. Teitelbaum, S. L. Bone resorption by osteoclasts. *Science* **289**, 1504–1508 (2000).
2. Teitelbaum, S. L. & Ross, F. P. Genetic regulation of osteoclast development and function. *Nature Rev. Genet.* **4**, 638–649 (2003).
3. Karsenty, G. & Wagner, E. F. Reaching a genetic and molecular understanding of skeletal development. *Dev. Cell* **2**, 389–406 (2002).
4. Rosen, H. & Goetzl, E. J. Sphingosine 1-phosphate and its receptors: an autocrine and paracrine network. *Nature Rev. Immunol.* **5**, 560–570 (2005).
5. Cyster, J. G. Chemokines, sphingosine-1-phosphate, and cell migration in secondary lymphoid organs. *Annu. Rev. Immunol.* **23**, 127–159 (2005).
6. Bokoch, G. M., Katada, T., Northup, J. K., Ui, M. & Gilman, A. G. Purification and properties of the inhibitory guanine nucleotide-binding regulatory component of adenylate cyclase. *J. Biol. Chem.* **259**, 3560–3567 (1984).
7. Akbar, H., Cancelas, J., Williams, D. A., Zheng, J. & Zheng, Y. Rational design and applications of a Rac GTPase-specific small molecule inhibitor. *Methods Enzymol.* **406**, 554–565 (2006).
8. Spiegel, S., English, D. & Milstien, S. Sphingosine 1-phosphate signaling: providing cells with a sense of direction. *Trends Cell Biol.* **12**, 236–242 (2002).
9. Takuwa, Y. Subtype-specific differential regulation of Rho family G proteins and cell migration by the Edg family sphingosine-1-phosphate receptors. *Biochim. Biophys. Acta* **1582**, 112–120 (2002).
10. Mazo, I. B. *et al.* Hematopoietic progenitor cell rolling in bone marrow microvessels: parallel contributions by endothelial selectins and vascular cell adhesion molecule 1. *J. Exp. Med.* **188**, 465–474 (1998).
11. Mazo, I. B. *et al.* Bone marrow is a major reservoir and site of recruitment for central memory $CD8^+$ T cells. *Immunity* **22**, 259–270 (2005).
12. Jung, S. *et al.* Analysis of fractalkine receptor CX_3CR1 function by targeted deletion and green fluorescent protein reporter gene insertion. *Mol. Cell. Biol.* **20**, 4106–4114 (2000).
13. Niess, J. H. *et al.* CX_3CR1-mediated dendritic cell access to the intestinal lumen and bacterial clearance. *Science* **307**, 254–258 (2005).
14. Burnett, S. H. *et al.* Conditional macrophage ablation in transgenic mice expressing a Fas-based suicide gene. *J. Leukoc. Biol.* **75**, 612–623 (2004).
15. Sanna, M. G. *et al.* Sphingosine 1-phosphate (S1P) receptor subtypes $S1P_1$ and $S1P_3$, respectively, regulate lymphocyte recirculation and heart rate. *J. Biol. Chem.* **279**, 13839–13848 (2004).
16. Wei, S. H. *et al.* Sphingosine 1-phosphate type 1 receptor agonism inhibits transendothelial migration of medullary T cells to lymphatic sinuses. *Nature Immunol.* **6**, 1228–1235 (2005).
17. Liu, Y. *et al.* Edg-1, the G protein-coupled receptor for sphingosine-1-phoshate, is essential for vascular maturation. *J. Clin. Invest.* **106**, 951–961 (2000).
18. Allende, M. L. *et al.* G-protein-coupled receptor $S1P_1$ acts within endothelial cells to regulate vascular maturation. *Blood* **102**, 3665–3667 (2003).
19. Ferron, M. & Vacher, J. Targeted expression of Cre recombinase in macrophages and osteoclasts in transgenic mice. *Genesis* **41**, 138–145 (2005).

20. Filgueira, L. Fluorescence-based staining for tartrate-resistant acidic phosphatase (TRAP) in osteoclasts combined with other fluorescent dyes and protocols. *J. Histochem. Cytochem.* **52**, 411–414 (2004).
21. Stoller, P., Reiser, K. M., Celliers, P. M. & Rubenchik, A. M. Polarization-modulated second harmonic generation in collagen. *Biophys. J.* **82**, 3330–3342 (2002).
22. Yu, X., Huang, Y., Collin-Osdoby, P. & Osdoby, P. Stromal cell-derived factor-1 (SDF-1) recruits osteoclast precursors by inducing chemotaxis, matrix metalloprotease-9 (MMP-9) activity, and collagen transmigration. *J. Bone Miner. Res.* **18**, 1404–1418 (2003).
23. Katayama, Y. *et al.* Signals from the sympathetic nervous system regulate hematopoietic stem cell egress from bone marrow. *Cell* **124**, 407–421 (2006).
24. Matloubian, M. *et al.* Lymphocyte egress from thymus and peripheral lymphoid organs is dependent on S1P receptor 1. *Nature* **427**, 355–360 (2004).
25. Cyster, J. G. Chemokines, sphingosine-1-phosphate, and cell migration in secondary lymphoid organs. *Annu. Rev. Immunol.* **23**, 127–159 (2005).
26. Kappos, L. *et al.* Oral fingolimod (FTY720) for relapsing multiple sclerosis. *N. Engl. J. Med.* **355**, 1124–1140 (2006).
27. Tedesco-Silva, H. *et al.* FTY720 versus mycophenolate mofetil in de novo renal transplantation: six-month results of a double-blind study. *Transplantation* **84**, 885–892 (2007).
28. Kobayashi, K. *et al.* Tumor necrosis factor α stimulates osteoclast differentiation by a mechanism independent of the ODF/RANKL-RANK interaction. *J. Exp. Med.* **191**, 275–286 (2000).
29. Ishii, M. *et al.* RANKL-induced expression of tetraspanin CD9 in lipid raft membrane microdomain is essential for cell fusion during osteoclastogenesis. *J. Bone Miner. Res.* **21**, 965–976 (2006).
30. Okamoto, H. *et al.* Inhibitory regulation of Rac activation, membrane ruffling, and cell migration by the G protein-coupled sphingosine-1-phosphate receptor EDG5 but not EDG1 or EDG3. *Mol. Cell. Biol.* **20**, 9247–9261 (2000).

Supplementary Information is linked to the online version of the paper at www.nature.com/nature.

Acknowledgements We thank U. H. von Andrian and I. B. Mazo for their help with the technique of intravital skull bone imaging. We also thank Y. Takuwa and N. Sugimoto for discussions, and P. M. Murphy and S.Venkatesan for their help in imaging *in vitro* chemotaxis using the EZ-Taxiscan. This work was supported in part by the Intramural Research Program of the National Institute of Allergy and Infectious Diseases, NIH, US Department of Health and Human Services, and by a fellowship grant to M.I. from the International Human Frontier Science Program.

Author Contributions M.I. performed most of experiments, with the assistance of J.G.E. and Y.S. for two-photon microscopy and for the *in vitro* osteoclast culture system, respectively. F.K. developed the unsupervised segmentation software and performed the computational analyses used to quantify the osteoclast-bone surface interface, with the assistance of M.M.-S. J.V. and R.L.P. generated *CD11b-Cre* transgenic and *S1PR1*$^{lox/P}$ knock-in mice, respectively. R.N.G. helped M.I. in designing and interpreting experiments, as well as in writing the paper.

Author Information Reprints and permissions information is available at www.nature.com/reprints. Correspondence and requests for materials should be addressed to R.N.G. (rgermain@niaid.nih.gov).

METHODS

Cell culture. The RAW264.7 cell line and mouse BM-MDM cells, which contain osteoclast precursor cells, were cultured as previously described[28,29]. To stimulate osteoclastogenesis, 50 ng ml^{-1} RANKL (PeproTech) was added to the medium and the cells were incubated for 3 to 4 days.

Conventional and quantitative RT–PCR amplification. Conventional RT–PCR was performed as described previously[29]. Primers used are listed in Supplementary Table 4. Relative quantification with real-time RT–PCR was performed using an ABI PRISM 7900 (Applied Biosystems Inc.) with an Assay-on Demand TaqMan probe and relevant primers, according to the manufacturer's instructions.

Determination of Rac activity. Pulldown assay methods to determine the GTP-bound active form of Rac have been described in detail previously[30].

***In vitro* chemotaxis chamber assay.** Chemotactic migration of cells was measured in a modified Boyden chamber as described previously[27].

EZ-Taxiscan chemotaxis assay. Chemotaxis experiments were also conducted in an EZ-Taxiscan chamber according to the manufacturer's protocol (Effector Cell Institute). The EZ-Taxiscan is a visually-accessible chemotactic chamber, in which one compartment containing ligand (S1P) and another compartment containing cells are connected by a microchannel. Phase contrast images of migrating cells were acquired at 1 min intervals.

Mice. C57BL/6 mice, CX_3CR1–EGFP knock-in mice[12], CSF1R (M-CSF receptor)–EGFP transgenic mice[14], were obtained from The Jackson Laboratory. The generation of the loxP-flanked *S1PR1* allele (*S1PR1*^{loxP})[18] and osteoclast/monocyte lineage-specific *CD11b-Cre* transgenic mice[19] were described previously. *S1PR1*$^{+/+}$ × *CD11b-Cre* and *S1PR1*$^{loxP/+}$ × *CD11b-Cre* littermates were born at expected frequencies and were viable and fertile, but live *S1PR1*$^{loxP/loxP}$ × *CD11b-Cre* littermates were obtained rarely (three viable *S1PR1*$^{loxP/loxP}$ × *CD11b-Cre* out of 59 total mice), suggesting possible embryonic lethality as seen with global $S1P_1$ deficiency. All mice were bred and maintained under specific pathogen-free conditions at animal facilities of NIH. Mutant mice were genotyped by PCR[18,19]. All mice were housed and handled according to NIH institutional guidelines under an approved protocol.

Immunohistochemistry. Immunohistological analyses were performed as described previously[2]. Anti-mouse $S1P_1$ rabbit polyclonal antibody was purchased from Affinity Bioreagents. In some experiments, fluorescence-based staining for TRAP[20] with ELF 97 substrate (Molecular Probes) was used with some modifications.

Two-photon intravital bone tissue imaging. Intravital microscopy of mouse calvaria bone tissues was performed using a protocol modified from a previous report[10,11]. Mice were anaesthetized with isoflurane (Baxter, 2.5% vaporized in an 80:20 mixture of oxygen and air), and the hair in the neck and scalp was removed with hair removal lotion (Nair). The frontoparietal skull was exposed and the mouse head was immobilized in a custom-made stereotactic holder. A catheter was placed into the tail vein with a 30-gauge needle attached to PE-10 tubing (Becton Dickinson). The imaging system was composed of an LSM510 NLO multiphoton microscope (Carl Zeiss) driven by a Chameleon XR Ti:Sapphire laser (Coherent) tuned to 880 nm, and an inverted microscope (Axiovert 200; Carl Zeiss) equipped with a ×40 water immersion objective (Achroplan IR, NA 0.8; Carl Zeiss). Fluorescent cells were detected through a bandpass emission filter at 525/50 nm (for EGFP). Vessels were visualized by injecting 70 kDa Texas Red conjugated-dextran (detected using a 620/60 nm filter) intravenously immediately before imaging. Image stacks were collected at 3-μm vertical step size at a depth of 100–150 μm below the skull bone surface. For three-dimensional videos, four sequential image stacks were acquired at 3 μm z spacing to cover a volume of 154 × 154 × 9.0 μm. The time resolution was 1 min. Raw imaging data were processed with Imaris (Bitplane) with a Gaussian filter for noise reduction.

Ovariectomy and FTY720 treatment. Twelve 12-week-old female, ovariectomized or sham-operated, C57BL/6J mice were purchased from Charles River Laboratories. Mice were injected intraperitoneally either with FTY720 (3 mg kg^{-1}, Cayman Chemical) dissolved in a vehicle (PBS containing 5% acidified DMSO and 30% fatty acid-free BSA) or with vehicle only, daily for 4 weeks. The mice were then killed and femurs were excised and fixed. Uteri of all the animals were excised and were weighed to evaluate the effect of ovariectomy.

Bone histomorphometry. Trabecular bone morphometry within the metaphyseal region of distal femur was quantified using micro-CT (μCT40, Scanco Medical AG). Volumeric regions for trabecular analysis were selected within the endosteal borders to include the central 80% of vertebral height and secondary spongiosa of femoral metaphyses located ~6% of the total length from the growth plate. Trabecular morphometry was characterized by measuring the bone volume fraction (bone volume/total volume), trabecular thickness and trabecular number. To assess the attachment of osteoclasts to the bone surface, osteoclasts and bone trabeculae were fluorescently visualized in sections by two-photon microscopy. To identify osteoclasts, fluorescence based TRAP staining[20] was performed. Collagen-enriched bone matrices could be visualized using the second harmonic emission from collagen fibres excited by infrared lasers. Sections were examined using a two-photon laser microscope (laser was tuned to 780 nm). Fluorescence was detected through bandpass emission filters at 370–450 nm (for second harmonic emission from bone matrices) or 525/50 nm (for TRAP staining). Image analysis was performed using a fully automated segmentation approach (no manual tracing of cell/tissue boundaries or other user intervention required) and the 'osteoclast attachment ratio' was calculated as the ratio 'bone surface attached by osteoclasts/total bone surface' (F.K., submitted manuscript).

Flow cytometry. All reagents were purchased from BD PharMingen. To examine the composition of PMCs, blood was collected from the retro-orbital plexus with a heparinized glass pipette, from mice treated intraperitoneally 4 h previously with FTY720 (3 mg kg^{-1}) or vehicle (Fig. 4), or treated intravenously 1 h previously with SEW2871 (5 mg kg^{-1}) or vehicle (Supplementary Fig. 4). After removing the red blood cells using ACK lysis buffer (Invitrogen), cells were stained with Alexa647-conjugated anti-F4/80 (Fig. 4), or FITC-conjugated anti-CD11b and PE-Cy7-conjugated anti-CD3 (Supplementary Figs 4 and 9), using conventional methods. Flow cytometric data were collected on a FACSCalibur (Becton Dickinson) and analysed with FlowJo software (TreeStar).

Quantifying cellular interaction dynamics in 3D fluorescence microscopy data

Frederick Klauschen[1,2], Masaru Ishii[3,4], Hai Qi[3], Marc Bajénoff[3,4], Jackson G Egen[3], Ronald N Germain[1,3] & Martin Meier-Schellersheim[1]

[1]Program in Systems Immunology and Infectious Disease Modeling, National Institute of Allergy and Infectious Diseases, National Institutes of Health, Bethesda, Maryland, USA. [2]Institute of Pathology, Universitätsmedizin Berlin, Berlin, Germany. [3]Lymphocyte Biology Section, Laboratory of Immunology, National Institute of Allergy and Infectious Diseases, National Institutes of Health, Bethesda, Maryland, USA. [4]Present addresses: Laboratory of Biological Imaging, Immunology Frontier Research Center (IFReC), Osaka University, 3-1 Yamada-oka, Suita 565-0871, Japan (M.I.), INSERM U924, Institut de Pharmacologie Moleculaire et Cellulaire, Centre National de la Recherche Scientifique, Université de Nice-Sophia-Antipolis, Valbonne, France (M.B.). Correspondence should be addressed to F.K. (fklauschen@mail.nih.gov) or M.M.-S. (mms@niaid.nih.gov).

Published online 20 August 2009; doi:10.1038/nprot.2009.129

The wealth of information available from advanced fluorescence imaging techniques used to analyze biological processes with high spatial and temporal resolution calls for high-throughput image analysis methods. Here, we describe a fully automated approach to analyzing cellular interaction behavior in 3D fluorescence microscopy images. As example application, we present the analysis of drug-induced and $S1P_1$-knockout-related changes in bone–osteoclast interactions. Moreover, we apply our approach to images showing the spatial association of dendritic cells with the fibroblastic reticular cell network within lymph nodes and to microscopy data regarding T–B lymphocyte synapse formation. Such analyses that yield important information about the molecular mechanisms determining cellular interaction behavior would be very difficult to perform with approaches that rely on manual/semi-automated analyses. This protocol integrates adaptive threshold segmentation, object detection, adaptive color channel merging, and neighborhood analysis and permits rapid, standardized, quantitative analysis and comparison of the relevant features in large data sets.

INTRODUCTION

The availability and usage of advanced fluorescence imaging techniques such as confocal and multi-photon microscopy have dramatically increased and enabled researchers to investigate biological processes with a high degree of spatial and temporal resolution. This includes, but is not limited to, studies ranging from static detection of the subcellular localization of proteins to dynamic tracking of fluorescent probes in single cells to intravital imaging of cell behavior in complex tissues and organs. These developments have been especially fruitful in fields such as immunology, cancer research and neuroscience, where the system behavior is largely governed by dynamic cell interactions, for instance, by the interactions between lymphocytes and antigen-presenting cells in lymph nodes[1–3], lymphocyte recruitment to and interaction with tumors[4] and synapse–glia dynamics in the brain[5]. Quantitative analysis of cell interaction behavior can considerably increase the information we can gain about the molecular mechanisms governing cellular communication processes or may be used to assess and quantify the efficacy of drugs. However, the development of computational high-throughput methods for automated and standardized quantitative analysis of the resulting 3D image data has lagged behind the experimental advances[6].

Here, we describe a protocol for the quantitative investigation of cell–cell, cell–tissue or cell–pathogen interactions that uses a fully automated, high-throughput image analysis method. The approach involves four steps that are carried out automatically without user intervention: First, the actual (true-positive) signal is separated from background (false-positive image elements) in each fluorescent image channel. Second, individual image objects are detected in the output data of the first step, which permits acquiring object numbers and size statistics and allows for the removal of image artifacts based on prior information about, for instance, minimum cell size. The third step merges the different fluorescent color channels to obtain an unambiguous segmentation. This step is especially important for interaction analyses because interfacing objects of different types (i.e., different colors) usually show a spatial image overlap that an accurate interface analysis must account for. Finally, in the last step, the interface areas are computed.

Advantages and disadvantages of our method

Previous approaches to interaction image analysis relied on semi-quantitative estimations using manual measurements of such features. For example, in conventional bone–osteoclast interaction analysis, data sets are sent to commercial labs and processed by personnel who manually delineate cellular boundaries and interfaces[7–11]. In contrast, the method presented here enables investigators to carry out rapid and standardized analyses that do not require operator interpretation in the vast majority of cases and are especially suited to the quantification of differences between experimental groups in large 3D data sets.

To assess the limitations and the usability of our protocol for different data types and image features, we tested different types of typical confocal/two-photon image data (see details below) that are acquired by different experimenters using different microscopy platforms. Moreover, we carried out sensitivity analyses by assessing the impact of the variation of the threshold selection parameter and the introduction of artificial image noise on the interface analysis. These tests showed that our approach works equally well for all data types we tested and that parameter/quality variations did not significantly affect the interface analysis results. However, we tested *typical* image data and noise. A limitation of the protocol (and segmentation approaches in general) is that excessive noise and/or

high background signal (approaching the intensity of the object signal) may lead to a failure of the ability of the method to separate noise/background from actual signal, which subsequently generates incorrect interface quantification results. As a rule of thumb, the protocol can be applied to image data whose intensity histogram meets the shape characteristics we describe. In contrast, the quality of the analysis can be expected to deteriorate when, for instance, the peak in the lower intensity region of the histogram representing the background 'collapses' into the higher intensity 'signal' region. However, we would like to point out that the main application of our protocol is the comparison of different experimental groups (e.g., see the following section) and that for this purpose (small) segmentation errors are acceptable as long as they occur consistently, which is guaranteed by our approach.

Example applications

The software we use in this protocol was initially developed for quantifying osteoclast–bone interactions in order to analyze how a $S1P_1$ (sphingosine-1-phosphate) receptor knockout mutant and the immunomodulatory drug FTY720 (Fingolimod, an $S1P_1$ agonist) that affect a lipid phosphate chemosensing pathway alter osteoclast activity *in situ*, thereby affecting bone homoeostasis[12]. We present this as our main example application and then show the versatility of the approach by describing its application to two other types of data. In the second example, we show how our approach can be used to analyze image data to quantify the extent to which dendritic cells attach to the fibroblastic reticular cell (FRC) networks on which T lymphocytes migrate within lymph nodes. The last example shows the applicability of the protocol for the investigation of interaction phenomena on a smaller scale: We analyze image data from recently published experiments[13] elucidating the influence of a mouse T-cell signaling mutation in the gene encoding SAP (signaling lymphocyte activation molecule (SLAM)-associated protein, the cause of X-linked lymphoproliferative syndrome (XLP)) on cell membrane contacts of T and B lymphocytes (this SAP mutation is known to affect the development of humoral immunity by influencing the stability of interactions between these T and B cells).

All these examples have in common that their analysis requires a quantitative assessment of either the size and/or the spatial localization of interfaces between cells or spatial regions with certain properties relevant for the biological question at hand, but differ in terms of size and shape of the cells and tissue structures.

The applications show the advantages of using an automated and standardized analysis method to perform unbiased comparisons of data sets that are obtained under different experimental conditions. As illustrated by the images in **Figures 1** and **2**, background fluorescence and the overlap between different color channels can make manual segmentation a challenging and subjective task. Under such conditions, variations in background signal/noise levels

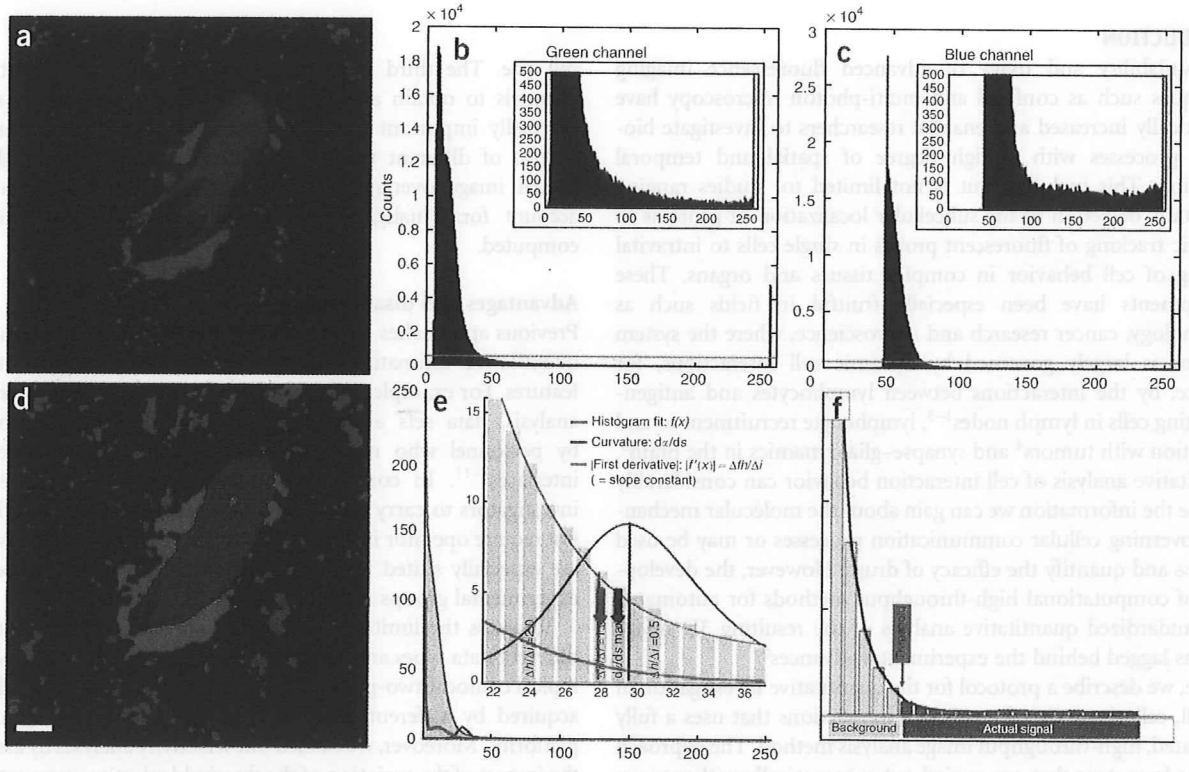

Figure 1 | Automated threshold segmentation. Example original (**a**) fluorescence two-photon image and intensity histograms showing the characteristic shape (**b**,**c**). Histograms can be divided into (1) a 'peak' region (lower intensity values) and (2) a 'constant' region stretching from the end of the 'peak' region to higher intensity values. (**b**) Osteoclasts (green) and (**c**) bone tissue (blue). (**d**) Resulting segmented image after automated thresholding using maximum curvature estimation method for threshold selection illustrated in panels **e** and **f**. (**e**) The curvature of the graph of the histogram fit (red) is shown in blue. Selection of the threshold at the curvature maximum is indicated by blue arrow. The approximation of the maximum curvature computation by the slope constant criterion $f'(x) \approx \Delta h/\Delta i = 1$ is depicted by the green curve and arrow. Scale bar = 10 μm. All animal procedures used in this study have been approved by the Animal Care and Use Committee, NIAID, NIH.

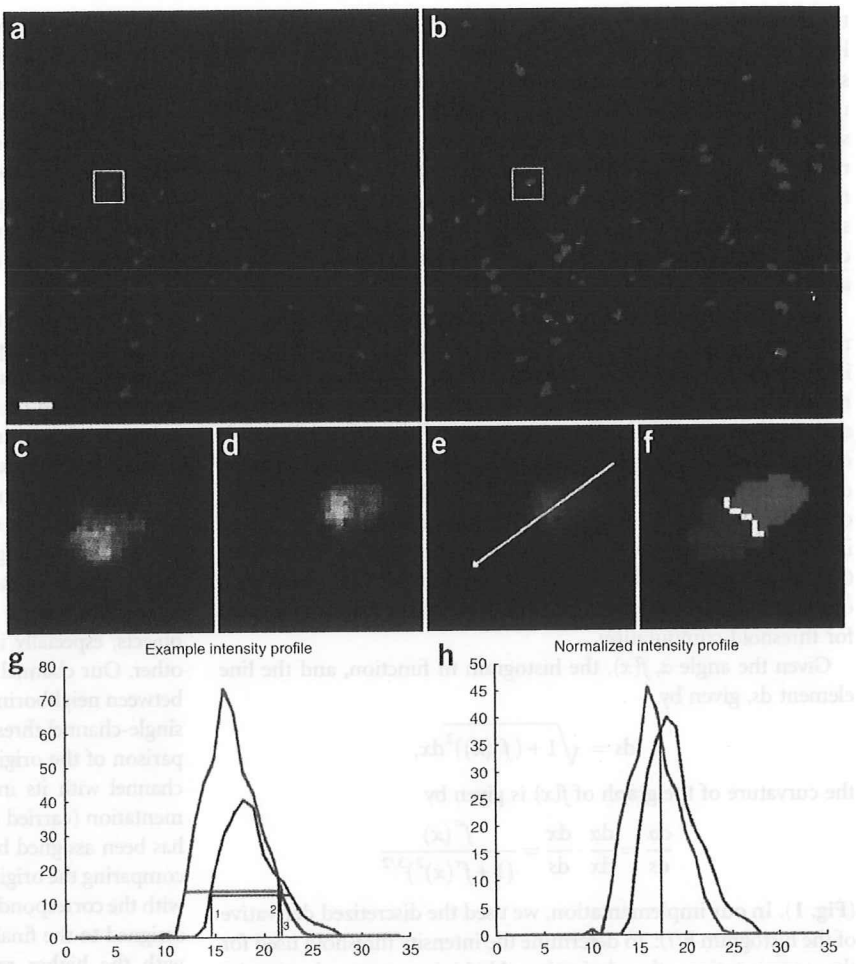

Figure 2 | Adaptive channel merging. (**a**) Original image data of T (green) and B (blue) cells. (**b**) Segmentation result, interacting T cells (red), interface (white). Magnification of blue (**c**) and green (**d**) channels with overlay (**e**) and segmentation result (**f**) from inset in panels **a** and **b**. Intensity profile along arrow in panel **e** is shown in panel **g**. Horizontal green and blue lines in panel **g** indicate computed threshold. Black vertical lines (1, 2 and 3) show the selection alternatives of the border between the blue and green channels under the condition that (1) either the blue or (3) the green object is given priority. Line 2 is the result of the border selection when comparing absolute intensities of competing channels. (**h**) Normalized intensity profile allows for balanced identification of the border between color channels (result shown in panel **f**). Scale bar = 10 μm. All animal procedures used in this study have been approved by the Animal Care and Use Committee, NIAID, NIH.

between data sets or between color channels in a single data set can easily mask subtle but significant biological differences or artificially create the impression of such differences. The potentially clinically relevant results obtained for the quantification of osteoclast–bone interaction robustly showed the ability of the immunomodulatory drug FTY720 to reduce the adhesion of osteoclasts to bone surfaces based on multiple data sets that display typical variations in image quality. This effect was not evident from visual inspection of the microscopy images and could be rigorously quantified only because of the adaptive standardization our protocol offers.

Detailed description of the image analysis program

The image analysis program performs the following steps automatically.

First module: Signal background separation by automated adaptive threshold segmentation. The critical step in image segmentation is the separation of signal from background, which includes discrimination of different signals (colors) from one another when considering multicolor fluorescence data sets. The first module of the image processing software that is used here performs an automated adaptive intensity threshold segmentation based on the characteristics of fluorescence confocal or two-photon image data. Such intensity histograms show a peak in the lower intensity region that represents the background signal, while the actual image signal is—relative to the form of the background part—approximately uniformly distributed over the (higher) intensity spectrum. We found this to be characteristic of all two-photon and confocal fluorescence microscopy images we analyzed and distinct from most conventional (non-fluorescent) image data (as in ref. 14) (**Fig. 1**). As the exact shape and location of the peak and a constant region vary depending on the image acquisition features, a stable and reliable segmentation method capable of yielding comparable results has to adapt to these variations that may occur between different as well as within individual data sets. The segmentation algorithm used here accomplishes this by defining the transition point between background and actual signal (i.e., the threshold), as the intensity value at which the curvature of the histogram graph is maximal (see 'Automatic adaptive thresholding: maximum curvature estimation' for details). In contrast to fully (3D) global thresholding methods with a single constant or user-selected cutoffs for the whole 3D image data set, our approach computes the threshold for each image *z*-slice separately and is therefore capable of compensating for intensity inhomogeneities (or 'attenuation') along the *z* axis (for instance, in deep-tissue two-photon imaging *in vivo*).

Automatic adaptive thresholding: maximum curvature estimation. In the case of photographic images, histograms often have a bimodal shape, with one peak representing background and the other signal portion of the image (**Supplementary Fig. 1**). In such cases, it is obvious that the threshold selection criterion is to find the minimum between the two peaks. There is no such criterion that is similarly obvious and also physically plausible in case of two-photon/confocal microscopy image data, and the transition between background and signal cannot be defined as a precise location similar to that in case of bimodal histograms. It can only be defined with some remaining degree of fuzziness in the region of

the transition between the strongly decaying part of the peak in the lower intensity spectrum and the region with the relatively flat slope. We chose the maximum curvature and its approximation using a derivative criterion for normalized histograms as threshold selection criterion, because it represents a mathematically definable, reasonable estimate of the transition point at which the strongly negative slope of the background peak changes to the relatively flat slope associated with the signal region and, moreover, because it is computationally efficient (alternative threshold selection criteria are discussed in ref. 14).

To compute the curvature of the (discrete) histogram in the relevant region, a Gaussian model may be used to fit the histogram in the relevant region, i.e., between global maximum (or local maximum with highest intensity value in the background region) and intensity 254. The maximum intensity histogram bin 255 is omitted in all calculations, because it is significantly higher than the other 'true positive' intensity values. This is due to the aggregation of all intensities ≥ 255 in this bin. We also omit the 0 bin, because in the case of image data of a low overall intensity (and thus many 0-intensity voxels) its inclusion may interfere with the generation of a normalized histogram that exhibits the shape features required for threshold computation.

Given the angle α, $f(x)$, the histogram fit function, and the line element ds, given by

$$ds = \sqrt{1 + (f'(x))^2}dx,$$

the curvature of the graph of $f(x)$ is given by

$$\frac{d\alpha}{ds} = \frac{d\alpha}{dx} \cdot \frac{dx}{ds} = \frac{f''(x)}{(1+f'(x)^2)^{3/2}}$$

(**Fig. 1**). In our implementation, we used the discretized derivative of the histogram $h(i)$: To determine the intensity threshold used for the segmentation, the derivative $\Delta h/\Delta i$ is computed stepwise starting at i=254 with decreasing i until the transition from the constant image to the non-constant background region is encountered. Before determining the threshold, the histogram is smoothed using a Gaussian filter (0 bin is the maximum bin of intensity histogram) scaled by the histogram integral and multiplied by a factor of 255 in order to normalize for the different cell/bone tissue coverage of the image area. Owing to the common histogram shape features present in all data sets, this scaling/normalization procedure resulted in the value of the discrete derivative

$$\frac{\Delta h}{\Delta i} = \frac{h(i-\Delta i) - h(i)}{\Delta i}$$

to be $\sim$1 at the maximum curvature point (**Fig. 1e**). Our sensitivity analysis of the precise location of the selected threshold (for details see 'Robustness assessment: Impact of variations of the slope constant on the interface area results') shows that this approximation is valid. **Supplementary Figure 2** shows an exemplary threshold segmentation result overlaid with the original image.

Second module: Object detection using connected component analysis. Following the automated thresholding procedure, our approach uses a 3D connected component labeling algorithm (see ref. 15 and references within) to identify individual image objects. The connected component labeling permits computation of the numbers of objects (such as cells) and the corresponding object features such as volume, surface area and location. It is also required for obtaining detailed information on cell–cell interaction behavior (e.g., the number of cells of type A attached to cells of type B) and for comparing features of potential interest of interacting versus non-interacting cells. In addition to the utility of the connected component analysis for the quantification of object features, our software also uses this analysis to improve image quality by applying a threshold filter for cell volumes, thus allowing removal from the processed data set of small pieces of cell debris or bright specks resulting from artifactual dye labeling.

Third and fourth modules: Channel merging and interface area computation using normalized intensity comparison and voxel-neighborhood analysis. The third step of the analysis pipeline finalizes the segmentation by adaptively merging the earlier separate segmentations of individual color channels. This is a pivotal step because most current image data involve objects (cells, pathogens and tissue components) that are labeled with different colors and whose fluorescent signals overlap when those objects are in close proximity, resulting in overlap in the segmentations of the individual color channels. Disregarding this issue may lead to distorted interaction results and even to the accidental removal of small objects, especially if one channel is significantly dimmer than the other. Our channel merging approach accounts for spatial overlap between neighboring or interacting image objects by combining the single-channel thresholding results with an adaptive intensity comparison of the original image data based on normalization of each channel with its intensity profile. After the initial threshold segmentation (carried out for each channel separately), each voxel that has been assigned both class labels ('overlap voxel') is evaluated by comparing the original image intensities in each channel normalized with the corresponding maximum intensity values. The voxel is then assigned to the final segmentation class that represents the channel with the higher relative intensity at that particular voxel. This approach therefore allows for an accurate estimate of the actual interfaces (see **Fig. 2** and **Supplementary Fig. 3**).

Finally, the interface areas are computed by identifying those voxels in channel 1 that are direct neighbors of voxels in channel 2. We use the sum of the surface voxels as an estimate of the total contact area. This is sufficient because the analysis result is provided in terms of ratios of interface areas to total cell or tissue surface areas or in terms of comparisons of such areas between different experimental groups.

Robustness assessment: impact of variations of the slope constant and noise on the interface area results. The robustness of an image segmentation and analysis method toward variations of pre-set parameters and image quality is an important measure of its utility. Therefore, we carried out a sensitivity analysis to evaluate the impact of variations in the slope value that is used to identify the boundary between background and true image data. This analysis showed that the average ratio of the interface area/total surface area in two groups (bone–osteoclast gene knockout versus wild-type data) with 20 data sets each (each data set consisting of $\sim$10 x–y images of 512 $\times$ 512 pixels) changes only $\sim$10% even when varying the slope value by a factor of 2 in both directions for both channels. More importantly, the differences of the average area ratios between the control and knockout groups—which is the relevant result in this kind of analysis—show a negligible dependence on the variation of the characteristic slope (change of

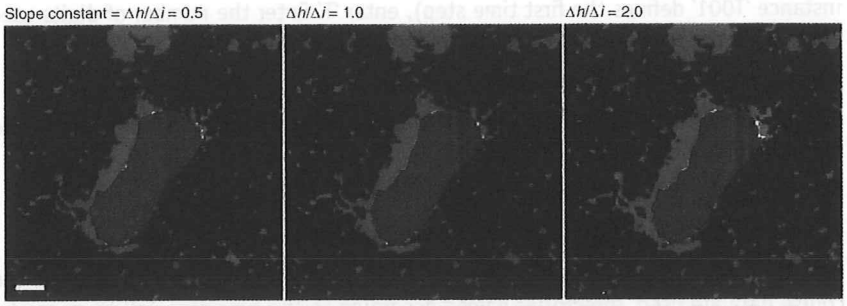

Figure 3 | Analysis of the impact of variations in the derivative constant on the normalized interface area (ratio of the interface area/total bone surface area) and on the difference between 'wild-type' and 'knockout' groups. Mean values are based on 20 data sets each in each group. Although changing the derivative constant by a factor of 2 in both directions relative to 1.0 results in average normalized interface area changes of ~10%, the differences change only 1.1% (0.5→1.0) and 2.2% (1.0→2.0). Scale bar = 10 μm. (For more information on the experiments see ref. 12.) All animal procedures used in this study have been approved by the Animal Care and Use Committee, NIAID, NIH.

	Normalized interface area (mean ± s.d.)		
Slope constant	0.5	1.0	2.0
Group 1 (wild type)	0.322 ± 0.151	0.369 ± 0.155	0.424 ± 0.157
Group 2 (knockout)	0.506 ± 0.181	0.551 ± 0.173	0.602 ± 0.162
Δ (group 1, 2)	0.184	0.182	0.178

difference is 1.1%; see **Fig. 3**). These results show that the particular choice of the slope value is less important than using the same constant throughout the data analysis, which subsequently generates the proper adaptive threshold value. This ensures that variations of image quality within and between data sets are normalized, thus permitting the consistent comparison of different data sets.

In addition to testing our approach with different types of typical confocal and two-photon microscopy data, we assessed the robustness of the analysis under the influence of various noise levels. We generated different levels of artificial noise for an exemplary data set (image noise follows a Poisson distribution[16]). The comparison of the analysis results yielded interface area differences of ≤5% between different typical Poisson noise levels (for details see **Supplementary Fig. 4**). However, because of the combination of noise and background signal and the diversity of possible features of fluorescence microscopy data, we cannot provide straightforward rules to determine a priori which data our protocol will work with. Low data quality may lead to significant misclassification (see **Supplementary Fig. 5**), and we therefore advise the user to carry out tests and examine test results to estimate the suitability of the automated analysis using this protocol and/or to optimize the user-definable parameters for the particular data. However, for the main application of this protocol, the comparative analysis of interaction behavior, it is above all important that data processing is standardized and that the data sets that are to be compared are of roughly similar quality. In that case, segmentation errors within reasonable limits are not problematic for comparative analyses using our protocol because they occur consistently.

MATERIALS

REAGENTS

Images for analysis, see REAGENT SETUP for further information about required format and **Supplementary Methods** for information on how images were acquired for our example applications.

EQUIPMENT

- Software (see EQUIPMENT SETUP for details)
- *Standard 32-bit hardware.* The example analyses shown in this protocol were performed on an Intel Xeon Dual Core 3.0 GHz workstation with 16 GB memory running 64-bit SuSE Linux. ▲ CRITICAL Although the analyses can in principle be performed on the standard 32-bit hardware, the memory requirements may go beyond 4 GB depending on image size and the number of biological objects in the image data, and 64-bit workstations with 8 GB or more memory may be required.

REAGENT SETUP

Image data preparation The analysis module of the software we present and use in this protocol requires image data to be in 3-color (RGB) Portable Network Graphics ('.png') format, with the *z*-slices in files consecutively numbered and assigned a defined filename prefix, for instance, 'img001.png, img002.png, img003.png …'. Each *z*-stack has to be saved in a single directory that does not contain any entries other than the image files. If a 4D data set is analyzed, each time step is treated separately and saved in individual directories.

Note that because this protocol describes interactions between two types of biological objects, only two-color channels are relevant. Here, by convention, we use 'green' as the first and 'blue' as the second channel. Microscope acquisition software usually permits saving images in TIFF format files, with one file per color channel and slice (and in case of 4D data per time step) indicated by certain identifiers, for instance 'filenameprefix_T000_C0_Z000.tif,' where 'T', 'C' and 'Z' indicate time step, color channel and *z*-slice, respectively. The software '2PISA' offers a module to convert such data into the format described above, if this is not required the protocol should be started at Step 10.

Software The description of the analysis method we provide offers sufficient detail for its implementation with a suitable high-level scripting/programming language (e.g., MATLAB). However, we recommend using our implementation of the software '2PISA' (2-Photon Image Segmentation and Analysis), which can be obtained free of charge for non-commercial use from the authors (http://www3.niaid.nih.gov/labs/aboutlabs/psiim/computationalBiology/) and is available for most versions of Linux, Mac OS X and Windows. The software package is written in C/C++ using the Qt library. Although the current release of the software supports two-color images, the method can in principle handle an unlimited number of channels as long as each class has a unique color label. An OpenGL-capable system is required for full functionality.

PROCEDURE

Image data preparation

1| Start the program '2pisaloader' to prepare the data.

2| In the menu 'Data,' select 'Convert data.'

3| If the data one would like to convert is time course data, select 'yes' and enter the single character that identifies the nature of the image parameter of interest. If 'T' defines the time step identifier (which is followed by the time step number, for

instance 'T001' defines the first time step), enter 'T.' Enter the number of digits used to encode the time step: in case of 'T001,' enter '3.' If the data are not time course data proceed to Step 4.

4| Enter the number of *z*-slices.

5| Enter the number of digits used for *z*-slice coding. The *z*-stack number must be at the end of the filename before the image format suffix, for instance '...001.png.'

6| Select the first image file of channel 1 ('green' channel).

7| Select the first image file of channel 2 ('blue' channel).

8| Enter the directory in which the converted data will be saved. The software then starts the image file conversion. If time course data are used, directories named according to the time step will be generated within the directory defined and contain the data for each time step. Otherwise, the converted images are saved directly in the directory specified.

Performing data analysis

9| Start the software '2pisaloader.'

10| In the menu 'Data', select 'Start data analysis.'

? TROUBLESHOOTING

11| Select the directory that contains the image data. Depending on the content of the selected directory, the software will automatically determine whether a single set or multiple data sets are to be analyzed: If the selected directory contains subdirectories with image files, all subdirectories are processed. If no subdirectories are present, the analysis is limited to the files in the selected directory. As the program counts the number of files in each directory to determine the size of the *z*-stack, it is important that only the relevant images files are in the directory named following the convention described above (see 'Data preparation').

12| Enter the filename prefix. The prefix has to be the same for all images files within the selected directory and subdirectories. Subsequently, the fully automated segmentation and analysis process is started and does not require any further user interaction.

? TROUBLESHOOTING

Results

13| Locate the segmentation results. These will be saved in the same directories as the original images with the filename prefix 'result' followed by the *z*-slice identifier equivalent to that of the original image, for instance for 'originalimage100.png,' 'result100.png.' In addition to the resulting image files, each directory will contain a file ('Results.txt') providing detailed interaction statistics, such as the number of interfacing cells/tissue components, interface area relative to total surface area, interface area per interfacing component, etc. If multiple data sets/directories are analyzed simultaneously, the top-level directory will contain a file ('AllResults.txt') that combines the results of all data sets.

14| Directly read these files and/or import to statistics/spreadsheet software for further analysis or visualization.

● TIMING

The analysis time strongly depends on the size and composition of the data sets and the computer hardware. The approximate duration of the bone–osteoclast interaction analysis with 512 × 512 × ~20 data sets on an Intel Xeon 3.0 GHz/16 GB workstation running 64-bit Linux is in the order of several minutes.

? TROUBLESHOOTING

Step 10: Manual parameter optimization

Although the default settings for the fully automated processing of the data worked well for all data sets we tested, the user can override the default settings and manually adjust/set the parameters 'slope constant,' 'threshold value' and 'minimal object size' to account for specific data features and optimize the accuracy of the analysis. Manual parameter selection can be enabled in the 'Settings' menu.

Step 12: Memory limitations

If large image data sets containing large numbers of objects are analyzed, the memory of standard 32-bit hardware (maximum 4 GB memory) may be insufficient and the analysis process might be terminated. Although it is not possible to precisely determine the memory requirement for a given image size, because it partially depends on the number of image objects processed in the connected component module, a rough estimate is that data sets of size ~250 × 250 × 10 (width × length × height) with a number of components similar to that present in the lymphocyte example can in most cases be analyzed on 32-bit hardware, whereas data sets equal to or larger than ~500 × 500 × >20 (as is the case for the bone–osteoclast data) are likely to require more memory. As an alternative to using 64-bit hardware with sufficient memory (~8 to 16 GB), the data sets can also be split into smaller subsets that are then analyzed separately.